

Observation of superconductivity and its enhancement at the charge density wave critical point in LaAgSb₂

Kazuto Akiba,^{1,*} Nobuaki Umeshita,¹ and Tatsuo C. Kobayashi¹

¹*Graduate School of Natural Science and Technology,
Okayama University, Okayama 700-8530, Japan*

(Dated: October 14, 2022)

Abstract

We discover superconductivity (SC) in LaAgSb₂ at ambient pressure and its close correlation with a charge density wave (CDW) under pressure. The superconducting transition temperature (T_c) exhibits a sharp peak at the CDW critical pressure of 3.2 GPa. We demonstrate that the carriers inhabiting the Sb-square net is crucial not only in the formation of CDW but also in SC for their relatively strong electron-phonon coupling (EPC). Furthermore, theoretical EPC strength in pristine LaAgSb₂ cannot explain the observed peak with $T_c \sim 1$ K, which indicates that an additional mechanism reinforces SC only around the CDW critical pressure.

* akb@okayama-u.ac.jp

Correlation between the superconductivity (SC) and other orders can help identify the mechanism behind SC and offers insight to improve the superconducting transition temperature (T_c). A well-known example is the correlation between SC and magnetism. When a magnetic phase transition temperature is continuously suppressed toward absolute-zero temperature by an external parameter, the phase transition can be triggered even at 0 K, which is known as a quantum critical point (QCP). Around the QCP, various physical quantities demonstrate anomalous temperature (T) dependence due to the spin fluctuation [1], which is called non-Fermi liquid behavior. Interestingly, unconventional SCs have been observed near the pressure- (P -) induced QCP in several heavy fermion systems [2–4], which result in a dome-like superconducting phase in the T - P phase diagram. This suggests that the spin fluctuation plays an important role on the pairing mechanism in this material class.

Alternatively, the correlation between SC and charge density wave (CDW) has also attracted considerable attention. In several representative materials, the emergence of SC or substantial enhancement of T_c occurs near the CDW critical point [5–9], which is often associated with a non-monotonic change of power law in the ρ - T curve at low temperatures [6, 7]. Intriguingly, these phenomena have several similar features as those of the magnetic QCP case, which suggests that these two phenomena have a possible commonality. However, a lack of model materials has hindered the elucidation of the essential relationship between SC and CDW.

Herein, we focus on the layered intermetallic compound LaAgSb₂ as an ideal platform to achieve the aforementioned goals. At ambient pressure, LaAgSb₂ exhibits sequential CDW transitions at $T_{CDW1} = 210$ K and $T_{CDW2} = 190$ K [10, 11], whose critical pressures are determined as $P_{CDW1} \sim 3.2$ GPa and $P_{CDW2} \sim 1.7$ GPa, respectively [12]. Although the origin of CDW2 is not conclusive at present, CDW1 is assumed to be derived from the nesting within the characteristic hollow-shaped Fermi surface (FS) [11, 13, 14]. Previous studies have reported that the hollow-shaped FS exhibits Dirac-like linear dispersion at the Fermi level [15, 16]. The emergence of the linear band crossing in Sb- or Bi-square-net materials can be understood as a result of band folding associated with the 4⁴-net structure [17–19]. Intriguingly, isostructural compounds LaAuSb₂ [20] and LaCuSb₂ [21] show superconductivity at 0.6 K and 0.9 K respectively, the former of which coexists with CDW order. However, there has been no report on SC in LaAgSb₂ thus far.

In this Letter, we reported the discovery of bulk SC in LaAgSb₂ at ambient pressure

with $T_c \sim 0.3$ K. SC exhibited intimate correlation with CDW1 under high pressure, and T_c was significantly enhanced up to $T_c \sim 1$ K only around P_{CDW1} . The theoretical calculation demonstrated that the Sb-square net is crucial not only as a host of Dirac fermions and CDW1, but also as a primary superconducting layer. In addition, theoretical T_c of pristine LaAgSb₂ cannot reproduce the peak structure under pressure, which suggests that an additional reinforcement mechanism of SC activated only around the CDW critical point exists.

Single crystal of LaAgSb₂ were synthesized using the Sb self-flux method [10, 12]. Temperatures as low as 50 mK were realized using a homemade ³He/⁴He dilution refrigerator. High pressure was generated using an indenter-type pressure cell (IPC, $P < 4$ GPa) [22] and opposed-anvil-type pressure cell (OAPC, $P < 7$ GPa) [23]. Daphne oil 7474 [24] was used as a pressure medium. The pressure in the sample space was determined based on the T_c of Pb set near the sample. The resistivity measurements were performed using a Model 370 AC resistance bridge (Lake Shore Cryotronics, Inc.) following a standard four-terminal method. Magnetization measurements were performed using a DC superconducting quantum interference device (Tristan Technologies, Inc.). In the magnetization measurement, we did not intentionally apply an external magnetic field. The measurements were done in residual geomagnetic field. Specific heat was measured by the relaxation method. The details of the magnetization and specific heat measurements are described in the Supplemental Material [25]. For resistivity and magnetization measurements, the sample was shaped into rectangle with typical dimensions of $1 \times 0.5 \times 0.1$ mm³. For specific heat measurements, relatively large as-grown crystal (typically several tens of milligram) was used. First-principles calculations were performed by Quantum ESPRESSO package [26–28] using scalar-relativistic ultrasoft pseudopotentials. Electron-phonon coupling (EPC) and T_c were calculated using Wannier90 [29] and EPW [30] codes. The visualization of orbital projections on FS was performed by FermiSurfer [31]. Calculation and verification of the results are described in detail in the Supplemental Material [25].

Figure 1(a) shows the temperature dependence of the in-plane resistivity ρ [current within the (001) plane] at ambient pressure. The residual resistivity ratio deduced from ρ at 300 K and 0.6 K was ~ 88 , and $T_{CDW1} = 210$ K was clearly observed (not shown). As depicted in Fig. 1(a), an abrupt decrease in ρ was observed, whose onset temperature can be defined as $T_c^{onset} = 0.29$ K, indicated by the arrow. This observation strongly suggests that the

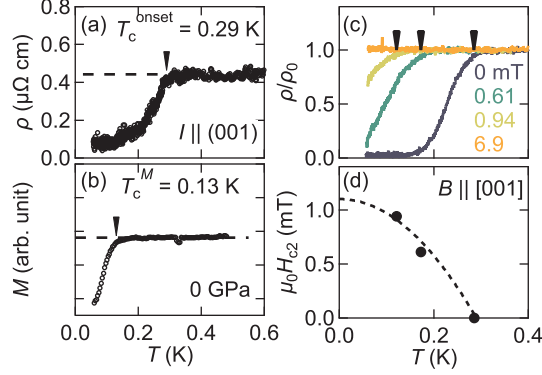


FIG. 1. (a) Temperature dependence of the in-plane resistivity ρ at ambient pressure. The onset temperature of the superconducting transition is determined as $T_c^{onset} = 0.29$ K. (b) Temperature dependence of the magnetization M at ambient pressure. The onset of the magnetization anomaly is determined as $T_c^M = 0.13$ K. (c) Temperature dependence of ρ normalized by the value at 0.4 K (ρ_0) under several external magnetic fields. Solid arrows indicate the onset of superconducting transition. (d) Temperature dependence of the upper critical field $\mu_0 H_{c2}$ obtained from the data shown in (c). The dashed line represents $\mu_0 H_{c2}$ (mT) = $1.1[1 - (T/0.29)^2]$.

superconducting state exists at ambient pressure.

Figure 1(b) plots the temperature dependence of the magnetization M for identical sample, which shows distinct anomaly at $T_c^M = 0.13$ K. In addition, the superconducting volume fraction was estimated as $\sim 39\%$ at 60 mK, as described in Supplemental Material [25]. Since the present measurement corresponds to field-cooling under residual geomagnetic field, the estimated volume fraction can be regarded as lower limit. The incomplete shielding and apparent difference between T_c^M and T_c^{onset} are presumably due to imperfect zero-resistivity even at the lowest T and broad superconducting transition in this sample.

Figure 1(c) shows the temperature dependence of ρ normalized by the value at 0.4 K (ρ_0) under external magnetic fields along [001] (c) axis. We note that there is a sample dependence in the sharpness of the superconducting transition; in a sample investigated in Fig. 1(c), we can recognize more clear zero resistivity than Fig. 1(a). The onset temperature of superconducting transition is systematically decreases as the magnetic field increases, and SC is completely absent under 6.9 mT. We can estimate from Fig. 1(d) the upper critical field ($\mu_0 H_{c2}$) at 0 K as ~ 1.1 mT.

To obtain thermodynamic evidence, specific heat at ambient pressure was measured.

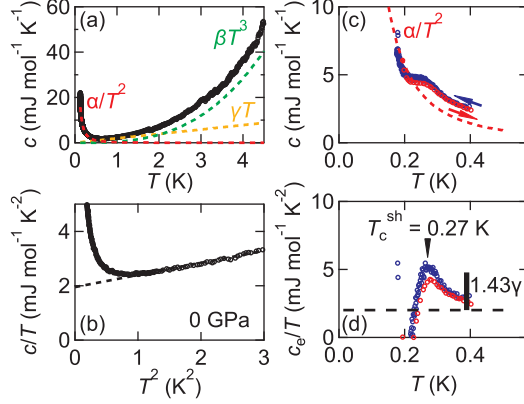


FIG. 2. (a) Temperature dependence of the specific heat c at ambient pressure. Dotted curves represent the individual contributions from nuclei (red), phonons (green), and electrons (orange). (b) c/T as a function of T^2 . The straight line represents the linear fit used for deducing the electron and phonon specific heat coefficients. (c) Specific heat anomaly below 0.5 K. Red and blue markers represent the heating and cooling processes, respectively. Dashed curve represents the nuclear contribution which is proportional to $1/T^2$. (d) c_e/T as a function of T , where c_e represents the electronic specific heat. Vertical scale represents the expected jump in BCS theory ($\sim 2.8 \text{ mJ mol}^{-1} \text{ K}^{-2}$).

Fig. 2(a) shows the temperature dependence of the specific heat c . c is represented as $c = \alpha/T^2 + \beta T^3 + \gamma T$, where the first, second, and third term represents the nuclear, phonon, and electron contribution, respectively. At relatively high temperature above 1 K, the nuclear contribution is negligibly small; thus, c is dominated by electron and phonon contributions. This results in the linear dependence in $c/T-T^2$ plot, as shown in Fig. 2(b). From the slope and vertical intercept of the straight line, $\beta = (444 \pm 7) \mu\text{J mol}^{-1} \text{ K}^{-4}$ and $\gamma = (1.95 \pm 0.01) \text{ mJ mol}^{-1} \text{ K}^{-2}$ were obtained. From β , the Debye temperature was estimated as $\Theta_D = (48R\pi^4/5\beta)^{1/3} = 260 \text{ K}$, where R represents the gas constant. The obtained γ and Θ_D are comparable to values reported in previous experiments [21, 32]. In contrast, at temperatures below 1 K, a drastic increase in nuclear contribution was observed, as shown in Fig. 2(a), which is well scaled by α/T^2 with $\alpha = (259.4 \pm 0.5) \mu\text{J mol}^{-1} \text{ K}$. By first-principles calculation, we confirmed notably large nuclear quadrupole resonance frequency of Sb due to large electromagnetic field gradient around Sb site, which is ascribed to be the origin of Schottky-type behavior below 1 K. Although the anomaly due to the superconducting transition is quite smaller than nuclear specific heat, a hump-like anomaly

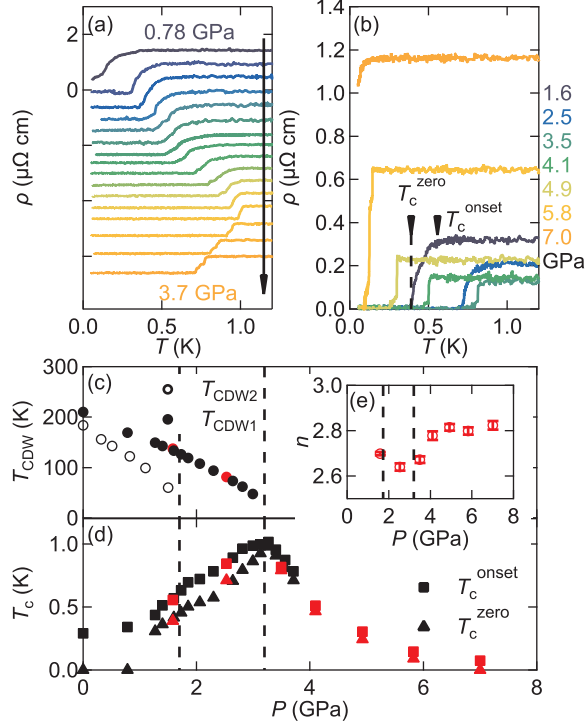


FIG. 3. Temperature dependence of ρ (a) up to 3.7 GPa measured using the indenter-type pressure cell (IPC) and (b) up to 7.0 GPa measured using the opposed-anvil-type pressure cell (OAPC). Each trace in (a) is vertically shifted for clarity. The definition of T_c^{onset} and T_c^{zero} are indicated by arrows in the case of 1.6 GPa in (b). Pressure dependence of (c) CDW transition and (d) superconducting transition temperatures. The black and red markers represent the data obtained using IPC and OAPC, respectively. (e) Pressure dependence of power n in $\rho = \rho_0 + A'T^n$ over the range $2.5 \text{ K} < T < 35 \text{ K}$.

can be discerned at $T_c^{sh} = 0.27 \text{ K}$, as shown in Fig. 2(c). Figure 2(d) shows c_e/T as a function of T , where the electronic specific heat c_e is obtained by subtracting the dashed curve in Fig. 2(c) from c . Magnitude of the anomaly shows reasonable agreement with $1.43\gamma \sim 2.8 \text{ mJ mol}^{-1} \text{ K}^{-2}$ [black vertical scale in Fig. 2(d)], which is expected from Bardeen-Cooper-Schrieffer (BCS) theory. This serves firm evidence for bulk SC at ambient pressure.

From the above results, the coexistence of the CDWs and SC in LaAgSb_2 at ambient pressure was established. Subsequently, their correlation under pressure was investigated.

Figure 3(a) and (b) show the temperature dependence of ρ up to 3.7 GPa and up to 7.0 GPa, obtained using IPC and OAPC, respectively. The pressure dependence of CDW and superconducting transition temperatures are summarized in Figs. 3(c) and 3(d), respectively.

The consistency of the data obtained by IPC and OAPC is satisfactory. Herein, T_{CDW1} was determined from the data presented in Supplemental Material [25], and T_{CDW2} was taken from our previous study [12]. The definitions of T_c^{onset} and T_c^{zero} are indicated in Fig. 3(b) by arrows. Although the transition was broad at pressures below 1 GPa, zero-resistivity above 1.3 GPa was distinctly observed. Both T_c^{onset} and T_c^{zero} gradually increased with pressure and reached their maxima almost exactly at $P_{CDW1} = 3.2$ GPa. Maximum onset temperature of $T_c^{onset} = 0.98$ K was found to be 3.4 times higher than that measured at ambient pressure. On the other hand, we can find no discernible anomaly at $P_{CDW2} \sim 1.7$ GPa. Above P_{CDW1} , T_c immediately got suppressed, and its decrement rate was steeper than the increment below P_{CDW1} . This resulted in a distinct peak structure in the T - P phase diagram, as shown in Fig. 3(d). At the highest pressure of 7.0 GPa, $T_c^{onset} = 75$ mK was 1/13 compared to its maximum value, and T_c^{zero} was again below the lowest limit of the present study. The obvious correlation with CDW1 further confirms the bulk SC.

Here, we discuss the correlation between CDW1 and SC. Because LaAgSb₂ is a non-magnetic material, the pairing mechanism is primarily assumed to be the EPC. Thus, we focused on the EPC strength in the momentum space at ambient pressure. In the following calculations, lattice modulation by CDWs was not considered, i.e., the results in pristine crystal structures without CDWs.

Figs. 4 (a) and (b) represent the distribution of the EPC strength $\lambda_{\mathbf{k}}$ on $k_z = 0$ and $k_z = \pi/c$ planes, respectively. Carriers with relatively strong EPC ($\lambda_{\mathbf{k}} \sim 0.3$) are concentrated on the two-dimensional hollow-like surface and elongated pocket at X point, whereas the rest of the FS exhibited weaker EPC ($\lambda_{\mathbf{k}} = 0.1$ – 0.15). As shown in Supplemental Material [25], this situation also holds under pressure. Because the hollow-like FS is the host of the CDW1 nesting, the abovementioned results lead to the interpretation that the CDW1 and SC compete on identical FS, which results in their remarkable correlation.

Figs. 4 (c) and (d) show the orbital characters of the FS on the k_z planes described in Figs. 4 (a) and (b). Notably the FSs with strong EPC are dominated by the intense $5p_{x,y}$ character of Sb1, which is a constituent of Sb-square net. The population of other orbitals were relatively minor, as presented in Supplemental Material [25]. These results indicate that the Sb-square net is responsible not only for the emergence of linear band crossing and nesting of CDW1 but also serves as a primary superconducting layer in this material. As we previously mentioned, no discernible anomaly of T_c at $P_{CDW2} \sim 1.7$ GPa was observed.

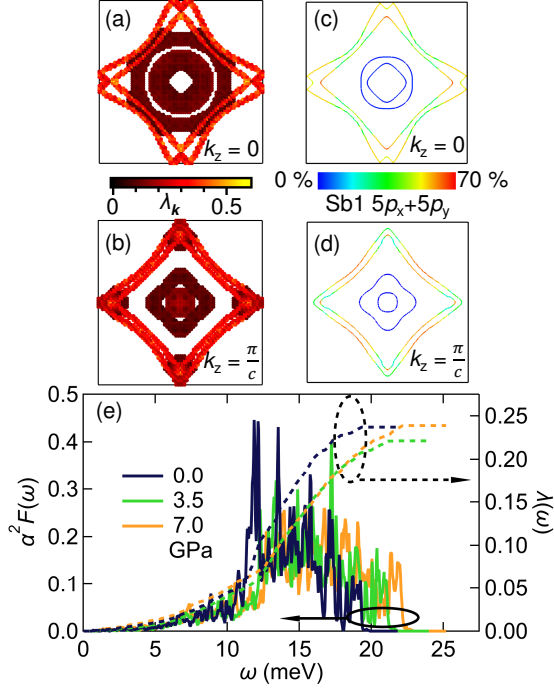


FIG. 4. Momentum-resolved electron–phonon coupling strength $\lambda_{\mathbf{k}}$ on (a) $k_z = 0$ and (b) $k_z = \pi/c$ planes at ambient pressure. $\lambda_{\mathbf{k}}$ is calculated for k points within the range of ± 0.2 eV from the Fermi level. The projection of $5p_x + 5p_y$ orbital character for Sb1 on (c) $k_z = 0$ and (d) $k_z = \pi/c$ planes at ambient pressure. (e) Eliashberg spectral function $\alpha^2F(\omega)$ (left axis) and integrated electron–phonon coupling strength $\lambda(\omega)$ (right axis) at 0, 3.5, and 7.0 GPa.

Given that the SC is primarily responsible for the Sb- $p_{x,y}$, this behavior can be reasonably understood. The lattice modulation accompanied by CDW2 is known to be along the c axis [11], which is perpendicular to the orbital spread; thus, a rather minor effect on SC is expected. In contrast, CDW1 causes lattice modulation along the a axis [11] within the Sb-square net, which can directly affect the superconducting properties.

Here, we extend our quantitative discussion on the superconducting properties based on McMillan–Allen–Dynes formalism [33–35]. Within this framework, the superconducting transition temperature T_c^{MAD} is represented as

$$T_c^{MAD} = \frac{\omega_{log}}{1.2} \exp\left(-\frac{1.04(1 + \lambda)}{\lambda - \mu_c^*(1 + 0.62\lambda)}\right), \quad (1)$$

where, $\lambda = \lambda(\omega_{max})$ is the integrated EPC strength defined by

$$\lambda(\omega) = 2 \int_0^\omega d\omega' \frac{\alpha^2F(\omega')}{\omega'}, \quad (2)$$

TABLE I. Theoretical EPC strength (λ), experimental EPC strength (λ^{exp}), logarithmic average of phonon frequency (ω_{log} , converted into temperature), and superconducting transition temperature estimated by McMillan–Allen–Dynes formula (T_c^{MAD}) with the Coulomb pseudopotential $\mu_c^* = 0.1$.

P (GPa)	λ	λ^{exp}	ω_{log} (K)	T_c^{MAD} (mK)
0.0	0.237	0.34	137.4	3.1
3.5	0.221	0.40	149.0	0.92
7.0	0.239	0.29	147.0	3.8

and ω_{log} is the logarithmic average of the phonon frequency defined as

$$\omega_{log} = \exp\left(\frac{2}{\lambda} \int_0^{\omega_{max}} d\omega \ln \omega \frac{\alpha^2 F(\omega)}{\omega}\right), \quad (3)$$

where ω_{max} denotes the maximum of the phonon frequency. $\alpha^2 F(\omega)$ is the Eliashberg spectral function, which can be obtained from first-principles results, as described in Supplemental Material [25]. The calculated $\alpha^2 F(\omega)$ at 0, 3.5, and 7.0 GPa are presented in Fig. 4(e) with corresponding $\lambda(\omega)$ values; the resulting λ , ω_{log} , and T_c^{MAD} are listed in Table I. To calculate T_c^{MAD} , we assumed a typical Coulomb pseudopotential of $\mu_c^* = 0.1$ for metals [36]. The obtained λ did not exhibit any notable pressure dependence. Accordingly, T_c^{MAD} was in the order of 1 mK at all pressures, which is three orders of magnitude smaller than the experimental maximum $T_c \sim 1$ K. Furthermore, theoretical upper limit of T_c could be calculated by setting $\mu_c^* = 0$, i.e., by completely disregarding the Coulomb interaction. The averaged upper limit was ~ 0.49 K, which is lower than the experimental maximum.

Here, we can deduce experimental EPC strength λ^{exp} based on [33]

$$\lambda^{exp} = \frac{1.04 + \mu_c^* \ln(\Theta_D/1.45T_c)}{(1 - 0.62\mu_c^*) \ln(\Theta_D/1.45T_c) - 1.04}. \quad (4)$$

Assuming $\Theta_D = 260$ K (estimated at ambient pressure), $\mu_c^* = 0.1$, and experimental T_c^{onset} , calculated λ^{exp} values are listed in Table I. At 7.0 GPa, far from P_{CDW1} , the difference between theoretical and experimental λ is small compared with other pressures, which supports the weak coupling nature of pristine LaAgSb₂. In contrast, near the P_{CDW1} , a λ nearly two times larger than the theoretical value is necessary to realize the observed maximum T_c assuming the EPC mechanism.

Consequently, the above results lead to a conclusion that there exists additional mechanism that significantly reinforces the SC only around P_{CDW1} . In the real case, the CDW

and superconducting gaps should compete for density of states on the FS below P_{CDW1} [37]. Although this conventional picture may partially account for the increasing trend of T_c below P_{CDW1} , it cannot explain significant difference in T_c between experiment and theory at P_{CDW1} and rapid decrease above P_{CDW1} .

Since above calculation does not explicitly consider the structural modification in the CDW states, we do not rule out an EPC origin, possibly related with a phonon softening by CDW1 formation [13, 38], at the present stage. Another possible mechanism is of electronic origin, i.e., a charge fluctuation around P_{CDW1} . Assuming a spin-singlet SC, the effective interaction of the Cooper pairs $V^s(\mathbf{k}, \mathbf{k}')$ is given by $V^s(\mathbf{k}, \mathbf{k}') = U + 3U^2\chi_s(\mathbf{k} - \mathbf{k}')/2 - U^2\chi_c(\mathbf{k} - \mathbf{k}')/2$ [39], where U , $\chi_s(\mathbf{k} - \mathbf{k}')$, and $\chi_c(\mathbf{k} - \mathbf{k}')$ represent Coulomb repulsion, spin susceptibility, and charge susceptibility, respectively. Since the increase of χ_c brings negative contribution on V^s , it can enhance the pairing attraction of the spin-singlet SC. Due to the coexistence of CDW1 and SC on identical FS and the absence of magnetism, the effect of charge fluctuation may stand out in the present case. We also note that a non-monotonic change in the exponent n in $\rho = \rho_0 + A'T^n$ was observed around 4 GPa, as shown in Fig. 3(e), which have been discussed in a context of possible quantum criticality at a CDW critical point [6, 7]. To distinguish above possibilities, further rigorous considerations on EPC and the role of charge fluctuation on SC around P_{CDW1} must be addressed, which is beyond the scope of the present study. The detailed mechanism of the reinforcement of SC is left as an open question for future study.

In conclusion, we observed the coexisting SC and CDW states in LaAgSb₂ at ambient pressure and their close correlation under high pressure. The EPC calculations revealed that the Sb-square net plays a vital role not only in the formation of linear band crossing and CDW1 but also in the emergence of SC. Our results highlight the strong reinforcement of SC activated only around the CDW1 critical point. LaAgSb₂ under high pressure serves an ideal platform to elucidate the essence of the correlation between SC and CDW and to seek a route to improve T_c based on critical points of charge orders.

ACKNOWLEDGMENTS

We thank J. Otsuki and H. Harima for valuable discussion and comments. This research was supported by JSPS KAKENHI Grants No. 19K14660, 21H01042, and 22K14006.

- [1] T. Moriya, *Spin Fluctuation in Itinerant Electron Magnetism* (Springer, Berlin, 1985).
- [2] R. Movshovich, T. Graf, D. Mandrus, J. D. Thompson, J. L. Smith, and Z. Fisk, *Phys. Rev. B* **53**, 8241 (1996).
- [3] F. Grosche, S. Julian, N. Mathur, and G. Lonzarich, *Physica B: Condensed Matter* **223-224**, 50 (1996).
- [4] N. D. Mathur, F. M. Grosche, S. R. Julian, I. R. Walker, D. M. Freye, R. K. W. Haselwimmer, and G. G. Lonzarich, *Nature (London)* **394**, 39 (1998).
- [5] E. Morosan, H. W. Zandbergen, B. S. Dennis, J. W. G. Bos, Y. Onose, T. Klimczuk, A. P. Ramirez, N. P. Ong, and R. J. Cava, *Nat. Phys* **2**, 544 (2006).
- [6] A. F. Kusmartseva, B. Sipos, H. Berger, L. Forró, and E. Tutiš, *Phys. Rev. Lett.* **103**, 236401 (2009).
- [7] T. Gruner, D. Jang, Z. Huesges, R. Cardoso-Gil, G. H. Fecher, M. M. Koza, O. Stockert, A. P. Mackenzie, M. Brando, and C. Geibel, *Nat. Phys.* **13**, 967 (2017).
- [8] K. Y. Chen, N. N. Wang, Q. W. Yin, Y. H. Gu, K. Jiang, Z. J. Tu, C. S. Gong, Y. Uwatoko, J. P. Sun, H. C. Lei, J. P. Hu, and J.-G. Cheng, *Phys. Rev. Lett.* **126**, 247001 (2021).
- [9] F. H. Yu, D. H. Ma, W. Z. Zhuo, S. Q. Liu, X. K. Wen, B. Lei, J. J. Ying, and X. H. Chen, *Nat. Commun.* **12**, 3645 (2021).
- [10] K. D. Myers, S. L. Bud'ko, I. R. Fisher, Z. Islam, H. Kleinke, A. H. Lacerda, and P. C. Canfield, *J. Magn. Magn. Mater.* **205**, 27 (1999).
- [11] C. Song, J. Park, J. Koo, K.-B. Lee, J. Y. Rhee, S. L. Bud'ko, P. C. Canfield, B. N. Harmon, and A. I. Goldman, *Phys. Rev. B* **68**, 035113 (2003).
- [12] K. Akiba, H. Nishimori, N. Umeshita, and T. C. Kobayashi, *Phys. Rev. B* **103**, 085134 (2021).
- [13] A. Bosak, S.-M. Souliou, C. Faugeras, R. Heid, M. R. Molas, R.-Y. Chen, N.-L. Wang, M. Potemski, and M. Le Tacon, *Phys. Rev. Research* **3**, 033020 (2021).
- [14] K. Akiba, N. Umeshita, and T. C. Kobayashi, *Phys. Rev. B* **105**, 035108 (2022).

- [15] K. Wang and C. Petrovic, *Phys. Rev. B* **86**, 155213 (2012).
- [16] X. Shi, P. Richard, K. Wang, M. Liu, C. E. Matt, N. Xu, R. S. Dhaka, Z. Ristic, T. Qian, Y.-F. Yang, C. Petrovic, M. Shi, and H. Ding, *Phys. Rev. B* **93**, 081105(R) (2016).
- [17] R. Hoffmann, *Angew. Chem. Int. Ed. Engl.* **26**, 846 (1987).
- [18] S. Klemenz, S. Lei, and L. M. Schoop, *Annu. Rev. Mater. Res.* **49**, 185 (2019).
- [19] S. Klemenz, A. K. Hay, S. M. L. Teicher, A. Topp, J. Cano, and L. M. Schoop, *J. Am. Chem. Soc.* **142**, 6350 (2020).
- [20] F. Du, H. Su, S. S. Luo, B. Shen, Z. Y. Nie, L. C. Yin, Y. Chen, R. Li, M. Smidman, and H. Q. Yuan, *Phys. Rev. B* **102**, 144510 (2020).
- [21] Y. Muro, N. Takeda, and M. Ishikawa, *J. Alloy. Compd.* **257**, 23 (1997).
- [22] T. C. Kobayashi, H. Hidaka, H. Kotegawa, K. Fujiwara, and M. I. Eremets, *Rev. Sci. Instrum.* **78**, 023909 (2007).
- [23] K. Kitagawa, H. Gotou, T. Yagi, A. Yamada, T. Matsumoto, Y. Uwatoko, and M. Takigawa, *J. Phys. Soc. Jpn.* **79**, 024001 (2010).
- [24] K. Murata, K. Yokogawa, H. Yoshino, S. Klotz, P. Munsch, A. Irizawa, M. Nishiyama, K. Iizuka, T. Nanba, T. Okada, Y. Shiraga, and S. Aoyama, *Rev. Sci. Instrum.* **79**, 085101 (2008).
- [25] See Supplemental Material at [URL].
- [26] P. Giannozzi, S. Baroni, N. Bonini, M. Calandra, R. Car, C. Cavazzoni, D. Ceresoli, G. L. Chiarotti, M. Cococcioni, I. Dabo, A. D. Corso, S. de Gironcoli, S. Fabris, G. Fratesi, R. Gebauer, U. Gerstmann, C. Gougoussis, A. Kokalj, M. Lazzeri, L. Martin-Samos, N. Marzari, F. Mauri, R. Mazzarello, S. Paolini, A. Pasquarello, L. Paulatto, C. Sbraccia, S. Scandolo, G. Sclauzero, A. P. Seitsonen, A. Smogunov, P. Umari, and R. M. Wentzcovitch, *J. Phys.: Condens. Matter* **21**, 395502 (2009).
- [27] P. Giannozzi, O. Andreussi, T. Brumme, O. Bunau, M. Buongiorno Nardelli, M. Calandra, R. Car, C. Cavazzoni, D. Ceresoli, M. Cococcioni, N. Colonna, I. Carnimeo, A. Dal Corso, S. De Gironcoli, P. Delugas, R. Distasio, A. Ferretti, A. Floris, G. Fratesi, G. Fugallo, R. Gebauer, U. Gerstmann, F. Giustino, T. Gorni, J. Jia, M. Kawamura, H. Ko, A. Kokalj, E. Küçükbenli, M. Lazzeri, M. Marsili, N. Marzari, F. Mauri, N. Nguyen, H. Nguyen, A. Otero-De-La-Roza, L. Paulatto, S. Poncé, D. Rocca, R. Sabatini, B. Santra, M. Schlipf, A. Seitsonen, A. Smogunov, I. Timrov, T. Thonhauser, P. Umari, N. Vast, X. Wu, and S. Baroni, *J. Phys.:*

- Condens. Matter **29**, 465901 (2017).
- [28] M. Kawamura, Y. Gohda, and S. Tsuneyuki, Phys. Rev. B **89**, 094515 (2014).
- [29] G. Pizzi, V. Vitale, R. Arita, S. Bluegel, F. Freimuth, G. Géranton, M. Gibertini, D. Gresch, C. Johnson, T. Koretsune, J. Ibanez, H. Lee, J.-M. Lihm, D. Marchand, A. Marrazzo, Y. Mokrousov, J. I. Mustafa, Y. Nohara, Y. Nomura, L. Paulatto, S. Poncé, T. Ponweiser, J. Qiao, F. Thöle, S. S. Tsirkin, M. Wierzbowska, N. Marzari, D. Vanderbilt, I. Souza, A. A. Mostofi, and J. R. Yates, J. Phys.: Condens. Matter **32**, 165902 (2020).
- [30] S. Poncé, E. Margine, C. Verdi, and F. Giustino, Comput. Phys. Commun. **209**, 116 (2016).
- [31] M. Kawamura, Comput. Phys. Commun. **239**, 197 (2019).
- [32] Y. Inada, A. Thamizhavel, H. Yamagami, T. Takeuchi, Y. Sawai, S. Ikeda, H. Shishido, T. Okubo, M. Yamada, K. Sugiyama, N. Nakamura, T. Yamamoto, K. Kindo, T. Ebihara, A. Galatanu, E. Yamamoto, R. Settai, and Y. Onuki, Phil. Mag. **82**, 1867 (2002).
- [33] W. L. McMillan, Phys. Rev. **167**, 331 (1968).
- [34] R. C. Dynes, Solid State Commun. **10**, 615 (1972).
- [35] P. B. Allen and R. C. Dynes, Phys. Rev. B **12**, 905 (1975).
- [36] P. Morel and P. W. Anderson, Phys. Rev. **125**, 1263 (1962).
- [37] G. Bilbro and W. L. McMillan, Phys. Rev. B **14**, 1887 (1976).
- [38] R. Y. Chen, S. J. Zhang, M. Y. Zhang, T. Dong, and N. L. Wang, Phys. Rev. Lett. **118**, 107402 (2017).
- [39] Y. Yanase, T. Jujo, T. Nomura, H. Ikeda, T. Hotta, and K. Yamada, Physics Reports **387**, 1 (2003).

Supplemental material for
”Observation of superconductivity and its enhancement at the
charge density wave critical point in LaAgSb₂”

Kazuto Akiba,^{1,*} Nobuaki Umeshita,¹ and Tatsuo C. Kobayashi¹

¹*Graduate School of Natural Science and Technology,
Okayama University, Okayama 700-8530, Japan*

(Dated: October 14, 2022)

Abstract

This Supplemental material includes 6 chapters, Figs. S1 to S13, and Table S1 to S2.

arXiv:2210.07175v1 [cond-mat.supr-con] 13 Oct 2022

* akb@okayama-u.ac.jp

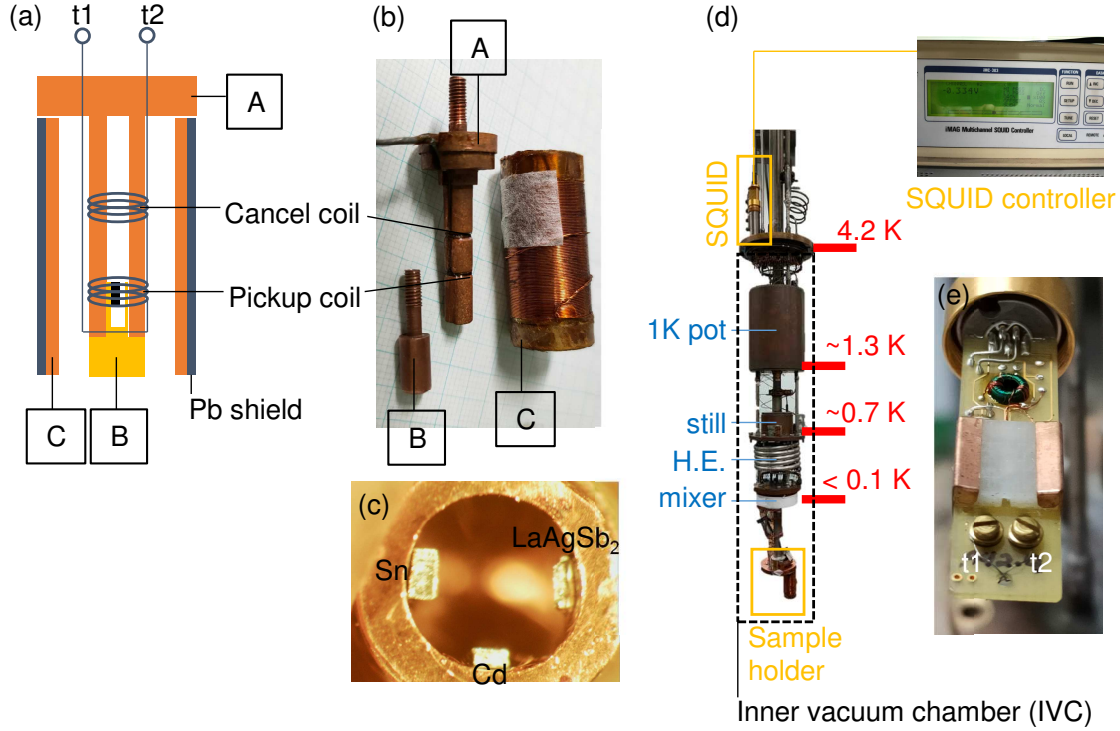


FIG. S1. (a) Schematic of the signal-pickup system for magnetization measurement. (b) Picture of the signal-pickup system. Parts A, B, and C correspond to those of (a). (c) Picture of the samples set inside part B. (d) Magnetization measurement system constructed on the dilution refrigerator. (e) Picture of the DC SQUID element utilized in this study.

I. MAGNETIZATION MEASUREMENTS

We describe the magnetization measurement system utilized in this study. Figures S1(a) and S1(b) show the schematic and actual picture of the measurement apparatus. All parts are made of copper. Part A has a pickup coil to detect the change in magnetic flux inside and cancel coil to reduce the background. These coils are wound by a superconducting NbTi wire. Part B can be screwed into part A and has a cylindrical sample space at the center. Samples are glued on the inner wall using Apiezon N grease (Fig. S1(c)). Part C is surrounded by a thin sheet of superconducting Pb to prevent the penetration of electronic noise from the outside. Although part C has a solenoid coil on the outermost layer to apply an external magnetic field, it has not been used here. These parts are set on the sample holder of the dilution refrigerator (Fig. S1(d)). The NbTi wire that starts from part A is shielded by a superconducting Nb tube and is taken out from the inner vacuum

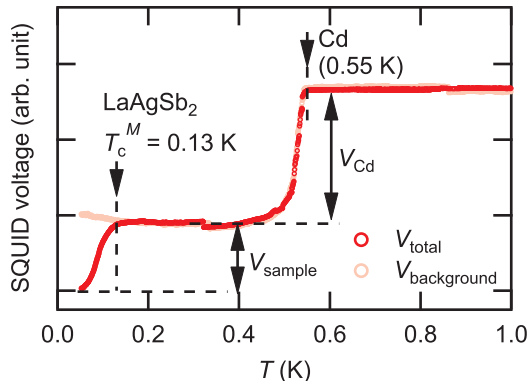


FIG. S2. Temperature dependence of the SQUID voltage below 1 K. V_{total} (red markers) indicates the data obtained by placing the LaAgSb_2 sample and Cd (reference) in the pick-up coil. $V_{background}$ (pink markers) indicates the data obtained by removing the sample from the above setup. The anomaly observed at 0.55 K is due to the Meissner effect of Cd.

chamber (IVC) of the refrigerator. The ends of the wire are tightened on the terminals of the DC SQUID element (labeled as t1 and t2 in Fig. S1(e)) that is manufactured by Tristan Technologies, Inc. The DC SQUID element is stored in a He bath, and hence its temperature is always held at 4.2 K. The DC SQUID element is connected with a controller via a communication cable. We can obtain the voltage signal on the controller, which is proportional to the change in the magnetic flux inside the pickup coil. We also note that we did not intentionally apply an external magnetic field. The situation corresponds to “field cooling in a residual geomagnetic field”.

Figure S2 shows the raw data to deduce the magnetization M of the sample. Note that we put a piece of Cd as a reference together with the LaAgSb_2 sample. Cd is known to be an elemental superconductor with a transition temperature of 0.56 K [1]. We measure the data with (V_{total}) and without ($V_{background}$) the sample. Upon lowering the temperature, we observe a sharp anomaly at 0.55 K in both V_{total} and $V_{background}$, which is almost identical to the known superconducting transition temperature of Cd. Upon further cooling, we can observe another anomaly that is found only in V_{total} , indicating the intrinsic magnetization response of the sample. We obtained the data shown in the main text by subtracting $V_{background}$ from V_{total} .

Using the data presented in Fig. S2, we can estimate the superconducting volume fraction. Here, we assume that the superconducting volume fraction of Cd is 100 %. Using the

known volume of the sample ($1.3 \times 10^{-4} \text{ cm}^3$), Cd ($1.0 \times 10^{-4} \text{ cm}^3$), and the signal ratio of $V_{sample} : V_{Cd} = 0.506 : 1$, where V_{sample} and V_{Cd} are defined in Fig. S2, the volume fraction of LaAgSb_2 is estimated to be 39 % at 60 mK.

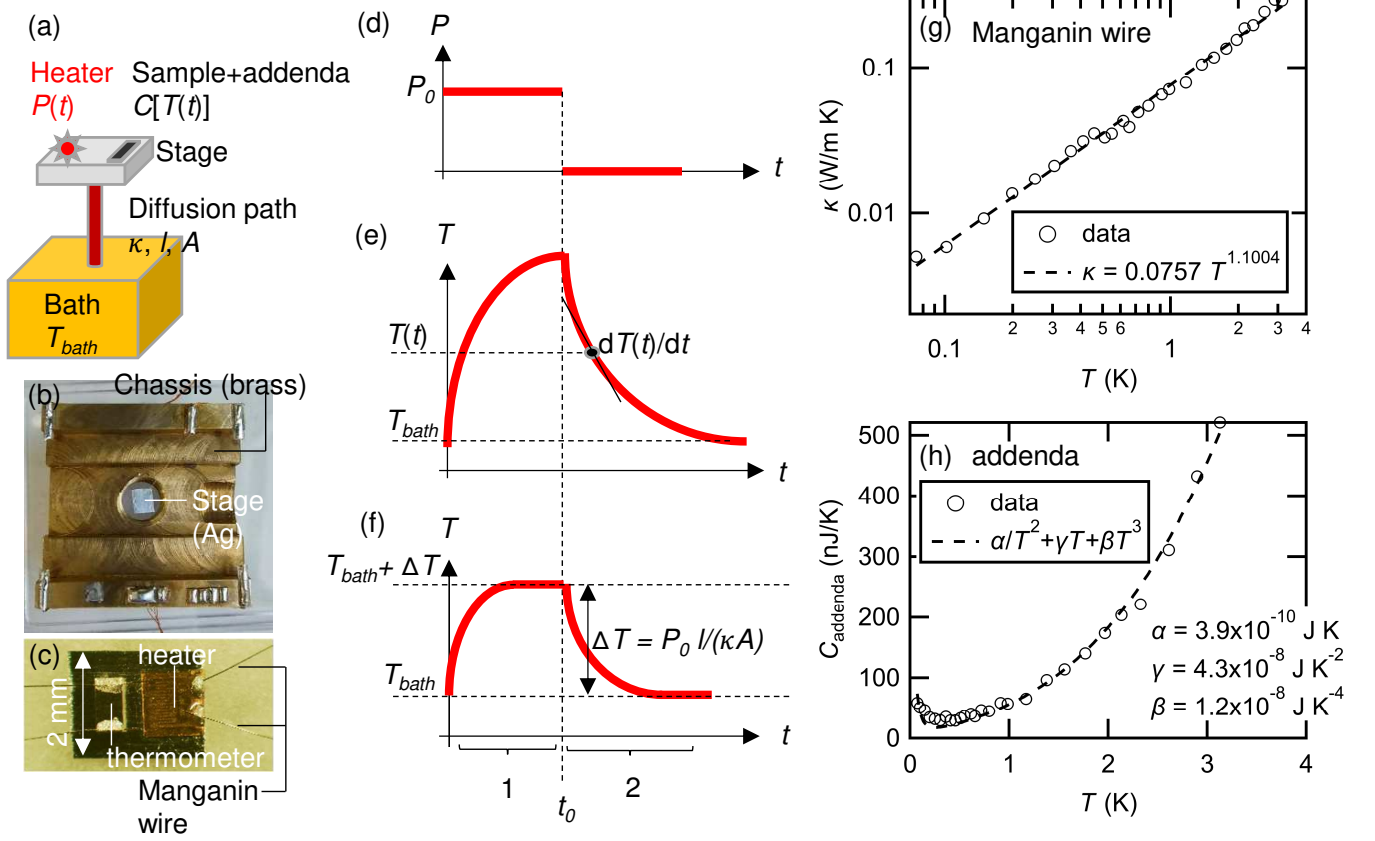


FIG. S3. (a) Schematic of the heat capacity measurement cell. Pictures of the (b) heat capacity measurement cell and (c) back of the sample stage. (d) Typical heater power applied to the stage as a function of time. (e) Typical temperature response measured by the thermometer in the sweep method. (f) Typical temperature response measured by the thermometer in the step method. (g) Temperature dependence of the thermal conductivity of the manganin wire. (h) Temperature dependence of the addenda heat capacity.

II. SPECIFIC HEAT MEASUREMENTS

We employed the relaxation method for the specific heat capacity measurements at low temperature. Figure S3(a) shows a schematic of the measurement cell. Figures S3(b) and S3(c) present the whole view of the measurement cell and a magnified view of the back of the sample stage, respectively. We used a piece of Ag ribbon or Si single crystal (The Nilaco Corporation) as a sample stage. The sample stage has a thermometer and a heater at the back as shown in Fig. S3(c). We utilized a commercial chip resistor (RK73B1ETTP202J, KOA Corporation) and a strain gauge (SKF-5414, Kyowa Electronic Instruments Co., Ltd.)

as a thermometer and heater, respectively. We calibrated the chip resistor for its use as a thermometer within the temperature range from 50 mK to 6 K prior to the measurements. The stage was weakly coupled with a thermal bath (chassis of the cell made of brass) through a thermal diffusion path. The actual diffusion path consisted of several manganin wires with diameters of 0.025 mm (The Nilaco Corporation). The cell was placed in the IVC of the dilution refrigerator, and thus thermal leakage through other paths was considered negligible.

Here, we explain the measurement principles. Assume that a constant electric power P_0 is applied to the heater at $t = 0$ and is turned off at t_0 (Fig. S3(d)). Correspondingly, the expected response of the sample temperature is schematically shown in Fig. S3(e). From the conservation of energy, the following relationship holds at arbitrary t :

$$P(t) = C[T(t)] \frac{dT(t)}{dt} + \frac{A}{l} \int_{T_{bath}}^{T(t)} \kappa(T') dT'. \quad (\text{S1})$$

Here, $P(t)$ is the electric power supplied by the heater and is either P_0 or 0. C is the combined heat capacity of the sample and addenda. $T(t)$ is the temperature at time t . T_{bath} is the temperature of the thermal bath and is monitored by a RuO₂ thermometer on the cell chassis. T_{bath} can be kept constant via feedback control using a heater tightened on the cell. A , l , and κ are the cross-section, length, and thermal conductivity of the diffusion path, respectively. From Eq. (S1), we can obtain the temperature dependence of C as follows:

$$C[T(t)] = \left[P(t) - \frac{A}{l} \int_{T_{bath}}^{T(t)} \kappa(T') dT' \right] / \frac{dT(t)}{dt}. \quad (\text{S2})$$

If the parameters P , A , l , T_{bath} , and $\kappa(T)$ are all known, we can obtain C at arbitrary t using the value of $dT(t)/dt$ obtained from the temperature response curve. This method is called the ‘‘sweep method’’.

Here, we consider another case where the temperature increase is small enough to assume C and κ as constants [Fig. S3(f)]. Thus, Eq. (S1) is solved analytically and we obtain

$$T(t) = T_{bath} + \frac{P_0 l}{\kappa A} (1 - \exp(-t/\tau)) \quad (\text{S3})$$

for time region 1 in Fig. S3(f) and

$$T(t) = T_{bath} + \frac{P_0 l}{\kappa A} \exp(-t/\tau) \quad (\text{S4})$$

for time region 2 in Fig. S3(f). For simplicity, we redefine t_0 as $t = 0$ in Eq. (S4). The relaxation time $\tau = Cl/(\kappa A)$ is directly dependent on C , and thus we can obtain C by curve

fitting procedures. κ contained in τ can be obtained from the temperature step ΔT as

$$\kappa = \frac{P_0 l}{\Delta T A}, \quad (\text{S5})$$

using the known P_0 , A , and l . This method is called the “step method”.

First, we obtained the temperature dependence of κ and addenda heat capacity $C_{addenda}$ using the step method. The typical ΔT is $\sim 1\text{-}10\%$ of T_{bath} . We observed the temperature response curves at various temperatures and obtained $\kappa(T)$ and $C_{addenda}(T)$ (Figs. S3(g) and S3(h)). As shown in Fig. S3(g), κ of manganin was observed in almost a straight line in the log-log plot, and thus we obtained the analytical expression as $\kappa(T) = 0.0757T^{1.1004}$ W/(m K) by curve-fitting. We also confirmed that $C_{addenda}(T)$ was reasonably reproduced by $C(T) = \alpha/T^2 + \gamma T + \beta T^3$, where the first, second, and third terms represent nuclear, electronic, and phononic contributions, respectively. Each coefficient obtained by curve fitting is listed in Fig. S3(h).

The expression of $\kappa(T)$ obtained in the above procedures allows us to evaluate the integration in Eq. (S2). Compared to the step method, denser data points were obtained over the wide temperature range from a single response curve via the sweep method, and thus it was advantageous to detect a rapid change in C accompanied by a phase transition. For this reason, we adopted the sweep method in this study.

The raw data to deduce c in the main text are listed in Fig. S4(a). We used the cooling of each data for the analysis. The plot of the obtained temperature dependence of C is shown in the inset of Fig. S4(a), in which the color corresponds to the raw response curves. After trimming the overlapped points, we subtracted $C_{addenda}$ from it to obtain the sample-heat capacity. Further, it was normalized by the molar amount of the sample, and finally, we obtained the specific heat c mentioned in the main text. The anomaly of c at the superconducting transition was obtained by another measurement using a different sample piece, and the relaxation curve is shown in Fig. S4(b). To check the specific heat anomaly at $T_c^{sh} = 0.27$ K, we calculated the specific heat from the heating and cooling curves and confirmed that the anomaly was reproducible in both processes as indicated in the main text.

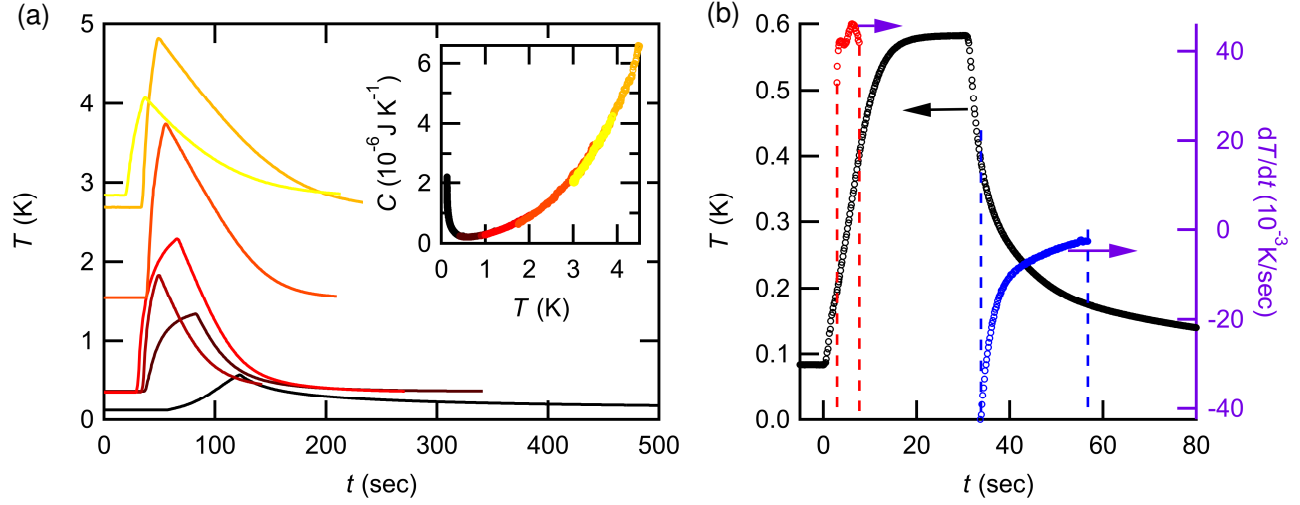


FIG. S4. (a) Temperature response curves ranging from 0.1 to 5 K. The inset shows the temperature dependence of the heat capacity obtained from the data shown in (a) using the sweep method. (b) Temperature response curve near the superconducting transition temperature. The right axis represents the time derivative of the response curve used in the sweep method.

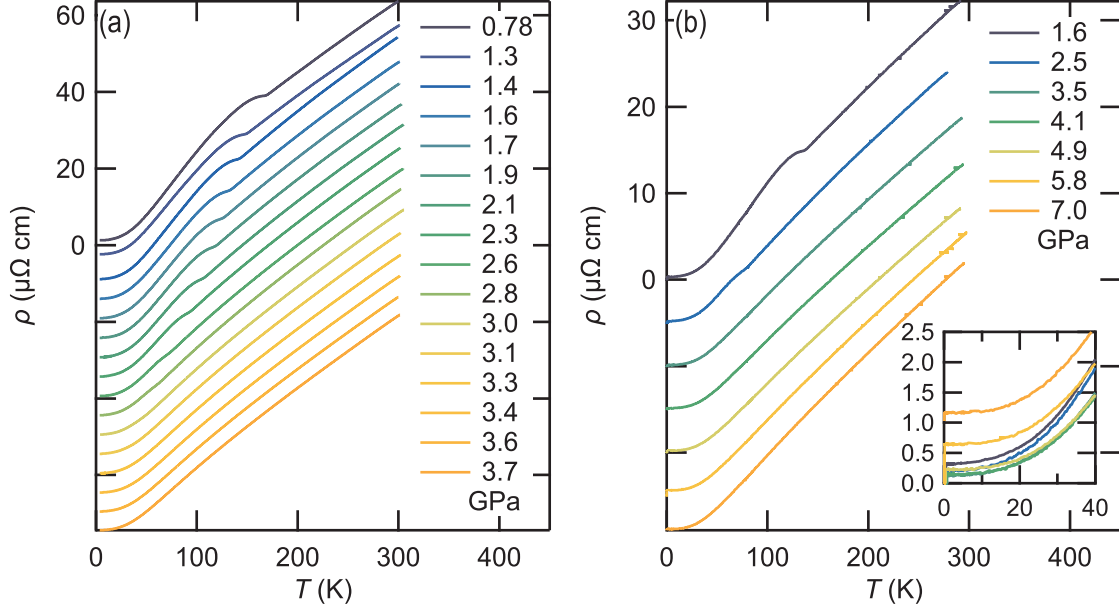


FIG. S5. (a) Temperature dependence of in-plane resistivity up to 300 K at various pressures up to 3.7 GPa measured using an indenter-type pressure cell. (b) Temperature dependence of in-plane resistivity up to 300 K at various pressures up to 7.0 GPa measured using an opposed-anvil-type pressure cell. The data are vertically shifted for clarity. The inset of (b) shows the magnified view below 40 K.

III. TEMPERATURE DEPENDENCE OF RESISTIVITY UP TO 300 K

Fig. S5 shows the plot of the temperature dependence of in-plane resistivity up to 300 K for all pressures investigated here. The data in the left and right panels were obtained using an indenter-type pressure cell and an opposed-anvil-type pressure cell, respectively. The inset of Fig. S5(b) shows the magnified view of the data obtained below 40 K. The power n of the temperature dependence was obtained by fitting the data shown in the inset with the fitting range from 2.5 K to 35 K.

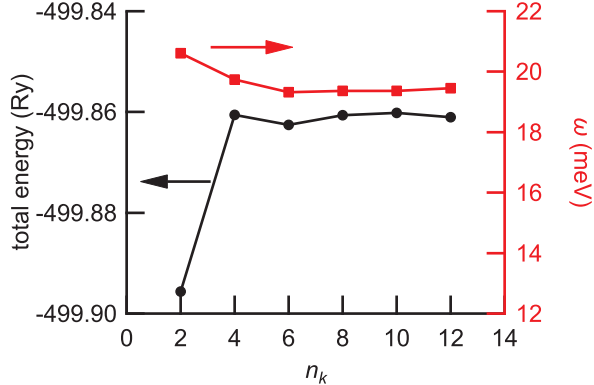


FIG. S6. Total energy of the electron system (left axis) and the highest optical phonon frequency at the Γ point (right axis) at ambient pressure calculated on the Γ -shifted n_k^3 Monkhorst-Pack k -point grids.

IV. FIRST-PRINCIPLES CALCULATIONS

The electronic structure calculations and structural optimization based on the density-functional theory (DFT) were performed by the Quantum ESPRESSO (QE) package [2, 3]. We used scalar-relativistic ultrasoft pseudopotentials with the Perdew-Burke-Ernzerhof exchange-correlation functional [4]. We set a cut-off of 75 and 540 Ry for the plane-wave expansion of the wave functions and charge density, respectively. Self-consistent calculations were performed with a threshold of 1.0×10^{-8} Ry. We evaluated the total energy at ambient pressure on several Γ -shifted n_k^3 Monkhorst-Pack k -point grids (Fig. S6) and adopted a Γ -shifted 6^3 k -mesh in terms of its accuracy and computational efficiency for subsequent calculations. For the structural optimization, internal atomic coordinates were relaxed in the fixed unit cell using convergence thresholds of 1.0×10^{-5} Ry for the total energy change and 1.0×10^{-4} Ry/Bohr for the forces. We adopted experimental lattice constants [5] for the calculation at ambient pressure. For calculations at 3.5 and 7.0 GPa, we used the lattice constants listed in Table S1, which were estimated from the experimental lattice compressibility [6]. Fully-relaxed positions for La (0.25, 0.25, z_{La}) and Sb2 (0.75, 0.75, z_{Sb2}) are also shown in Table S1. The atomic positions at ambient pressure show reasonable agreement with our experimental values $z_{La} = 0.23969$ and $z_{Sb2} = 0.33036$ [5]. From the density of states at ambient pressure, we could estimate the electron specific heat as $2.2 \text{ mJ mol}^{-1} \text{ K}^{-2}$, which was in agreement with our experimental value of $1.95 \text{ mJ mol}^{-1} \text{ K}^{-2}$.

TABLE S1. Lattice constants a and c used for the structural optimization and fully relaxed atomic coordinates for La (0.25, 0.25, z_{La}) and Sb2 (0.75, 0.75, z_{Sb2}).

P (GPa)	a (Å)	c (Å)	z_{La}	z_{Sb2}
0.0	4.3941	10.868	0.24071	0.32752
3.5	4.3495	10.556	0.24154	0.32428
7.0	4.3282	10.379	0.24219	0.32218

TABLE S2. Calculated phonon frequencies at Γ point (ω_{Γ}) at ambient pressure. ω_{Γ}^{ref} is taken from a previous calculation by Singha *et al* [7]. ω_{Γ}^{SO} is obtained by full-relativistic calculation. “I” and “R” in activity column represents infrared active and Raman active, respectively.

ω_{Γ} (meV)	ω_{Γ}^{ref} (meV)	ω_{Γ}^{SO} (meV)	mode	activity
0.00		0	A_{2u}	I
0.00		0	E_u	I
6.86	4.06	6.86	E_g	R
7.19		7.27	E_u	I
9.46		9.43	A_{2u}	I
10.84	7.80	10.73	E_g	R
11.06		11.09	E_u	I
12.01	12.3	12.04	B_{1g}	R
12.46	13.0	12.69	B_{1g}	R
12.55	12.4	12.80	E_g	R
13.02	13.4	12.84	A_{1g}	R
14.59	15.1	14.43	A_{1g}	R
15.93		15.98	A_{2u}	I
16.94		16.97	E_u	I
17.30		17.31	A_{2u}	I
19.32	20.2	19.29	E_g	R

The phonon calculations were performed based on the density functional perturbation theory (DFPT) with the optimized tetrahedron method [8] implemented in QE. A convergence threshold of 1.0×10^{-14} Ry was employed for the DFPT self-consistent iterations. As seen in Fig. S6, the highest optical phonon frequency at the Γ point at ambient pressure sufficiently converged on the adopted 6^3 k -mesh. The obtained frequency of 19.32 meV was consistent with the previous Raman experiment (18.7 meV) and calculation (20.2 meV) [7]. All calculated phonon frequencies at the Γ point at ambient pressure are listed in the ω_Γ column in Table S2. Although several modes with lower frequencies exhibited relatively significant differences compared to the previous calculation [7] (ω_Γ^{ref}), the overall correspondence seemed to be reasonable. The mismatch might be due to the difference in the utilized package and the adopted numerical condition. The phonon dispersions were calculated using a Γ -centered 4^3 q -point grid.

We plotted the (a) electron-band structure $\epsilon - \epsilon_F$, (b) electron density of states $D(\epsilon)$, (c) phonon-band structure ω , and (d) phonon density of states $D_{ph}(\omega)$ obtained by DFT/DFPT calculations in Figs. S7–S9 (black solid curves).

Here, we comment on the effect of spin-orbit coupling (SOC). In this study, we adopted scalar-relativistic calculations without SOC. In previous studies, it has already been shown that SOC causes only a slight change in the electronic band structure around the Fermi level [9, 10]. To test the effect of SOC on phonon properties, we calculated the phonon frequency at the Γ point using full-relativistic ultrasoft pseudopotentials, and its results are shown in the ω_Γ^{SO} column in Table S2. Compared with the scalar-relativistic case, the difference is only less than three percent for all modes, and thus we can adopt the scalar-relativistic calculation here.

From the theoretical phonon density of the state spectrum $D_{ph}(\omega)$, we can obtain the temperature dependence of the phonon specific heat $c_{ph}(T)$ as [11]

$$c_{ph}(T) = \int d\omega k_B \left(\frac{\hbar\omega}{k_B T} \right)^2 \frac{\exp\left(\frac{\hbar\omega}{k_B T}\right)}{\left[\exp\left(\frac{\hbar\omega}{k_B T}\right) - 1\right]^2} D_{ph}(\omega), \quad (\text{S6})$$

and the calculated $c_{ph}(T)$ at ambient pressure is represented in Fig. S10. We can evaluate the Debye temperature as 234 K by curve fitting at low temperature up to 6 K (inset of Fig. S10), which is consistent with our experimental value of 260 K. We also confirmed

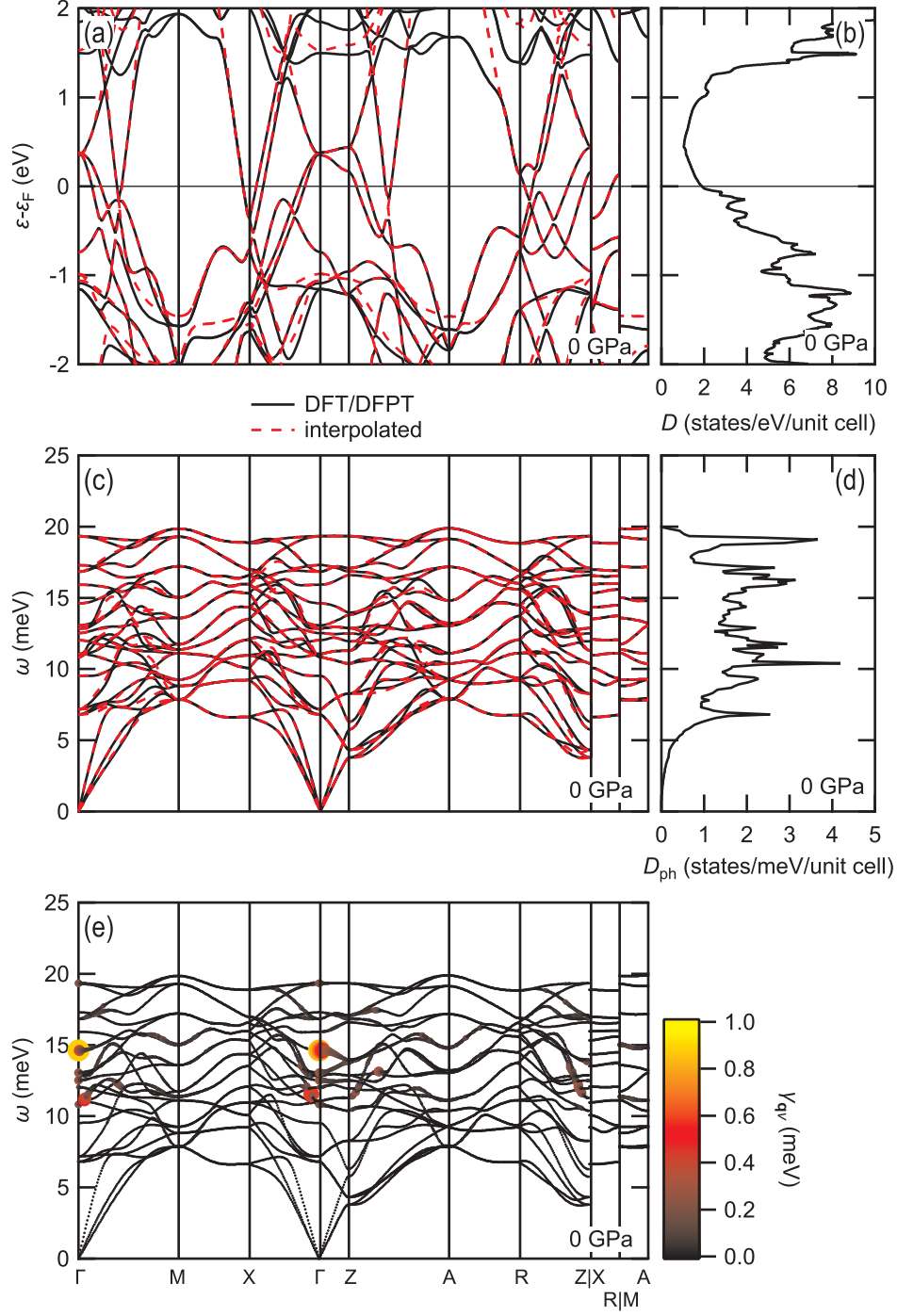


FIG. S7. (a) Electron-band structure, (b) electron density of states, (c) phonon-band structure, and (d) phonon density of states at 0 GPa. The solid black curves represent the DFT/DFPT results and red dashed curves represent the interpolated results. (e) Distribution of the phonon linewidth $\gamma_{q\nu}$ at 0 GPa. The color and size of the markers represent the magnitude of $\gamma_{q\nu}$.

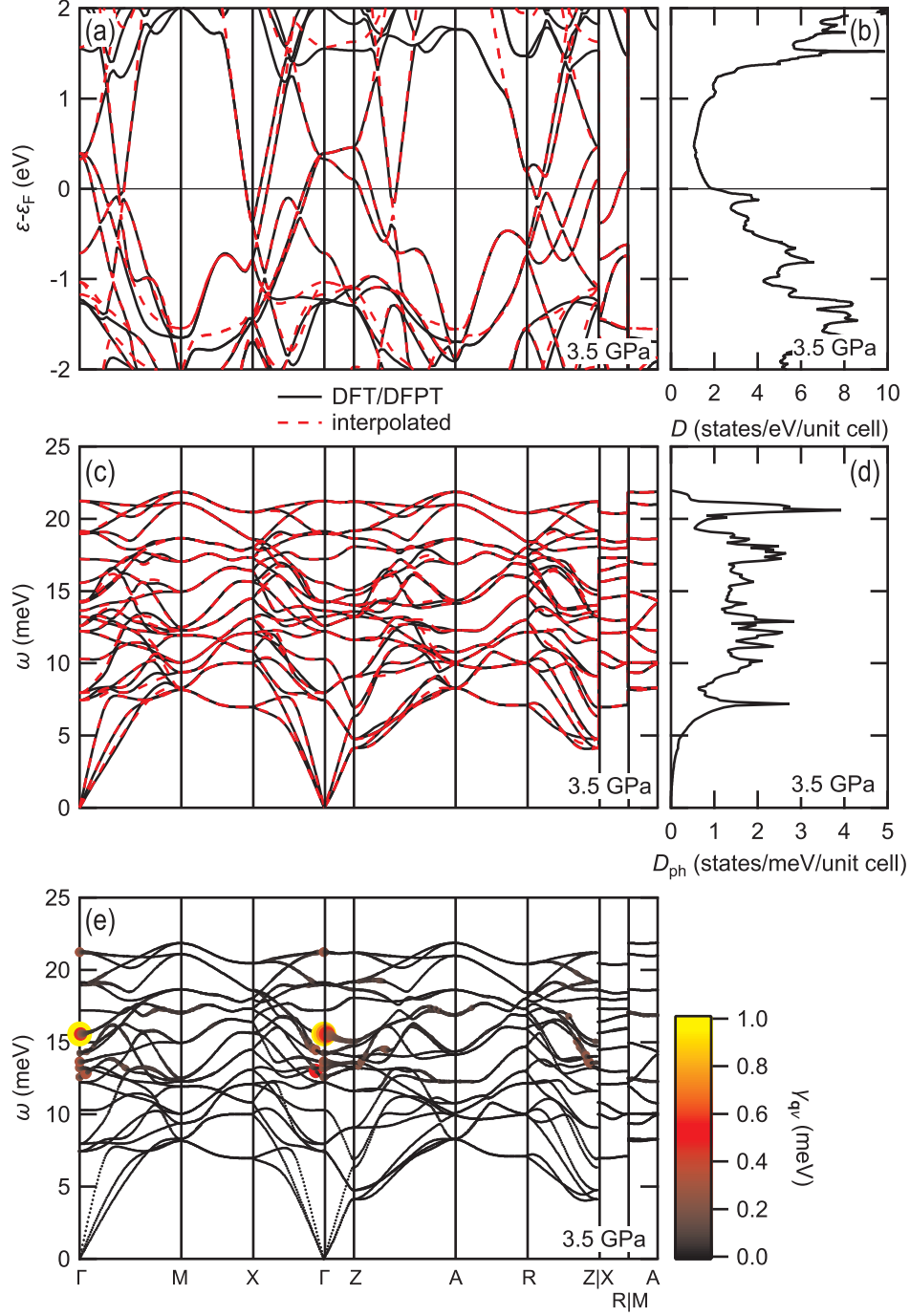


FIG. S8. (a) Electron-band structure, (b) electron density of states, (c) phonon-band structure, and (d) phonon density of states at 3.5 GPa. The solid black curves represent the DFT/DFPT results and red dashed curves represent the interpolated results. (e) Distribution of the phonon linewidth $\gamma_{q\nu}$ at 3.5 GPa. The color and size of the markers represent the magnitude of $\gamma_{q\nu}$.

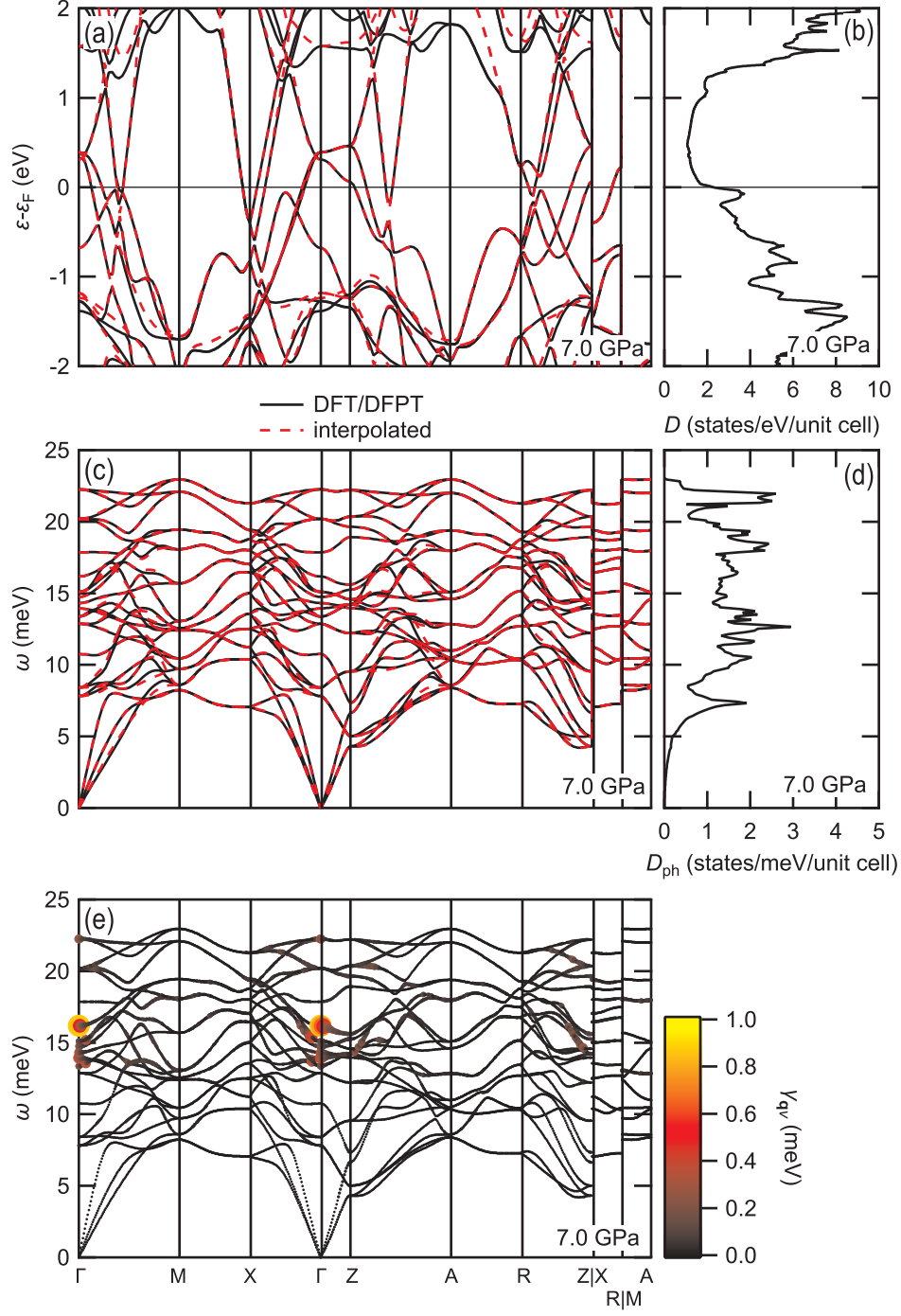


FIG. S9. (a) Electron-band structure, (b) electron density of states, (c) phonon-band structure, and (d) phonon density of states at 7.0 GPa. The solid black solid represent the DFT/DFPT results and red dashed curves represent the interpolated results. (e) Distribution of the phonon linewidth $\gamma_{q\nu}$ at 7.0 GPa. The color and size of the markers represent the magnitude of $\gamma_{q\nu}$.

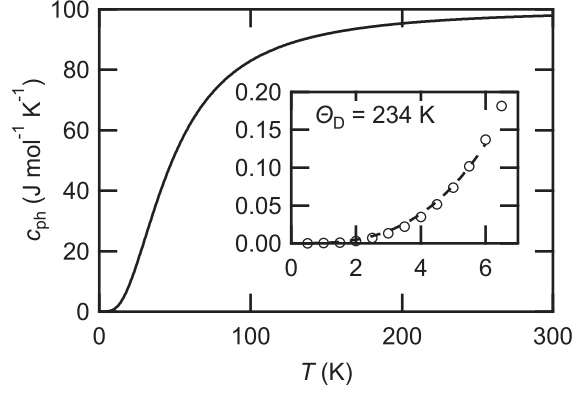


FIG. S10. Temperature dependence of the phonon specific heat calculated from the theoretical phonon density of states using Eq. (S6). The inset shows the magnified view of the low temperature region with fitting curves (dashed curve) assuming that $c_{ph} \propto T^3$.

quite satisfactory agreement with the previous heat capacity measurement up to 80 K [12]. The above consistencies with previously reported experiments confirm the validity of the calculated phonon properties.

V. ELECTRON-PHONON COUPLING CALCULATIONS

Based on the DFT and DFPT results, we calculated the electron-phonon coupling and phonon-mediated superconducting transition temperature using Wannier90 [13] and EPW [14] codes. The electron-phonon matrix element is defined as

$$g_{mn,\nu}(\mathbf{k}, \mathbf{q}) = \sqrt{\frac{\hbar}{2M\omega_{q\nu}}} \langle \Psi_{m\mathbf{k}+\mathbf{q}} | \partial_{\mathbf{q}\nu} V | \Psi_{n\mathbf{k}} \rangle. \quad (\text{S7})$$

Here, M and \hbar are the mass of the nuclei and reduced Planck constant, respectively. $\omega_{q\nu}$ represents the frequency of phonon with a wavevector \mathbf{q} and mode index ν . $|\Psi_{n\mathbf{k}}\rangle$ is the electronic wavefunction for band index n and wavevector \mathbf{k} with eigenvalue of $\epsilon_{n\mathbf{k}}$. $\partial_{\mathbf{q}\nu} V$ is the derivative of the self-consistent potential associated with a phonon having \mathbf{q} and ν . Using $g_{mn,\nu}(\mathbf{k}, \mathbf{q})$, the phonon linewidth $\gamma_{q\nu}$ and electron-phonon coupling strength $\lambda_{q\nu}$ associated with a phonon having ν and \mathbf{q} are represented as

$$\gamma_{q\nu} = 2\pi\omega_{q\nu} \sum_{nm} \int_{BZ} \frac{d\mathbf{k}}{\Omega_{BZ}} |g_{mn,\nu}(\mathbf{k}, \mathbf{q})|^2 \delta(\epsilon_{n\mathbf{k}} - \epsilon_F) \delta(\epsilon_{m\mathbf{k}+\mathbf{q}} - \epsilon_F), \quad (\text{S8})$$

$$\lambda_{q\nu} = \frac{2}{N(\epsilon_F)\omega_{q\nu}} \sum_{nm} \int_{BZ} \frac{d\mathbf{k}}{\Omega_{BZ}} |g_{mn,\nu}(\mathbf{k}, \mathbf{q})|^2 \delta(\epsilon_{n\mathbf{k}} - \epsilon_F) \delta(\epsilon_{m\mathbf{k}+\mathbf{q}} - \epsilon_F) = \frac{\gamma_{q\nu}}{\pi N(\epsilon_F)\omega_{q\nu}^2}. \quad (\text{S9})$$

Here, $N(\epsilon_F)$ is the density of states per spin at the Fermi level ϵ_F , and the integral is taken over the Brillouin zone with Ω_{BZ} volume. $\delta(\epsilon)$ represents the Dirac delta function. Alternatively, we can represent the electron-phonon coupling strength in the \mathbf{k} -space as

$$\lambda_{n\mathbf{k}} = \sum_{m\nu} \int_{BZ} \frac{d\mathbf{q}}{\Omega_{BZ}} \frac{2}{\omega_{q\nu}} |g_{mn,\nu}(\mathbf{k}, \mathbf{q})|^2 \delta(\epsilon_{m\mathbf{k}+\mathbf{q}} - \epsilon_F). \quad (\text{S10})$$

In the main text and hereafter, we omit the band index n and simply write as $\lambda_{\mathbf{k}}$.

Using $\lambda_{q\nu}$, the Eliashberg spectral function $\alpha^2 F(\omega)$ can be obtained by calculating its integrated value over the Brillouin zone as follows:

$$\alpha^2 F(\omega) = \frac{1}{2} \sum_{\nu} \int_{BZ} \frac{d\mathbf{q}}{\Omega_{BZ}} \omega_{q\nu} \lambda_{q\nu} \delta(\omega - \omega_{q\nu}). \quad (\text{S11})$$

Then, we estimated the superconducting transition temperature T_c^{MAD} using the McMillan-Allen-Dynes formula [15–17]

$$T_c^{MAD} = \frac{\omega_{log}}{1.2} \exp\left(-\frac{1.04(1+\lambda)}{\lambda - \mu_c^*(1+0.62\lambda)}\right). \quad (\text{S12})$$

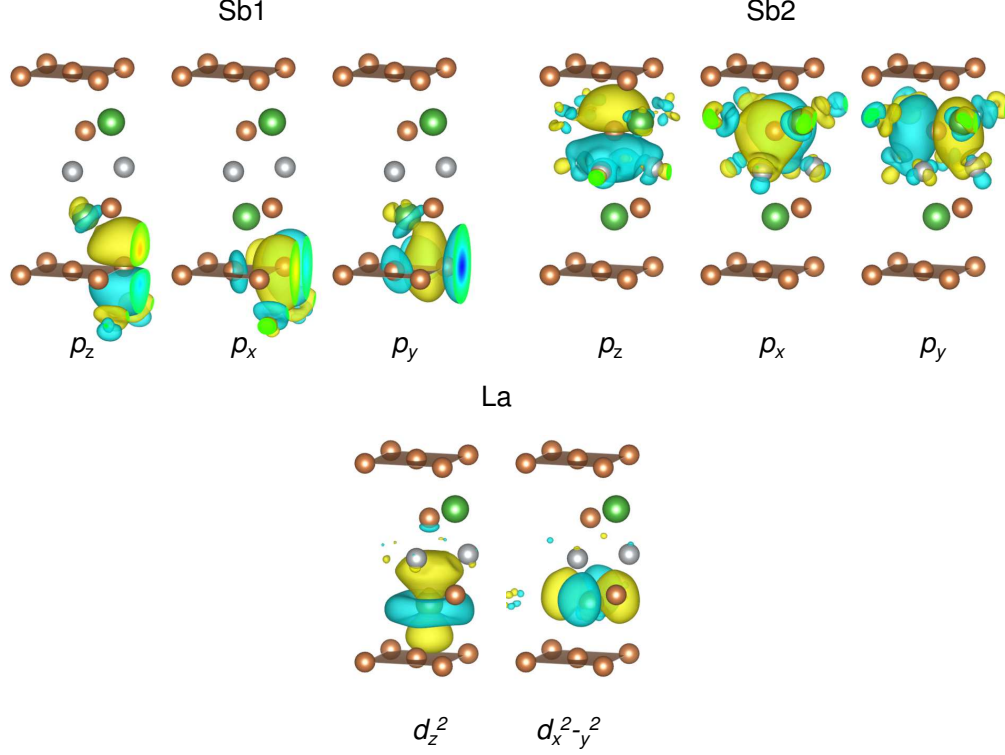


FIG. S11. Obtained maximally-localized Wannier orbitals at ambient pressure.

Here, λ is defined using the Eliashberg spectral function and maximum phonon frequency ω_{max} as

$$\lambda = 2 \int_0^{\omega_{max}} d\omega \frac{\alpha^2 F(\omega)}{\omega}, \quad (\text{S13})$$

and ω_{log} is a logarithmic average of the phonon frequency defined as

$$\omega_{log} = \exp \left(\frac{2}{\lambda} \int_0^{\omega_{max}} d\omega \ln \omega \frac{\alpha^2 F(\omega)}{\omega} \right). \quad (\text{S14})$$

μ_c^* represents the Coulomb pseudopotential, which is treated as an empirical parameter. For typical metals, μ_c^* is known to take values around 0.1 [18]. In the main text, we assumed $\mu_c^* = 0.1$.

We used coarse 8^3 k -mesh and 4^3 q -mesh for the initial calculation of the electronic Hamiltonian, dynamical, and electron-phonon matrices. To calculate the electron-phonon coupling properties on arbitrary dense Brillouin zone grids, an interpolation scheme described in [19] was applied using EPW. In this procedure, we used 16 maximally localized Wannier functions. We show in Figs. S7–S9(a–d) the comparison of DFT/DFPT band structures (black solid curves) and interpolated band structures (red dashed curves) at 0, 3.5, and 7.0 GPa,

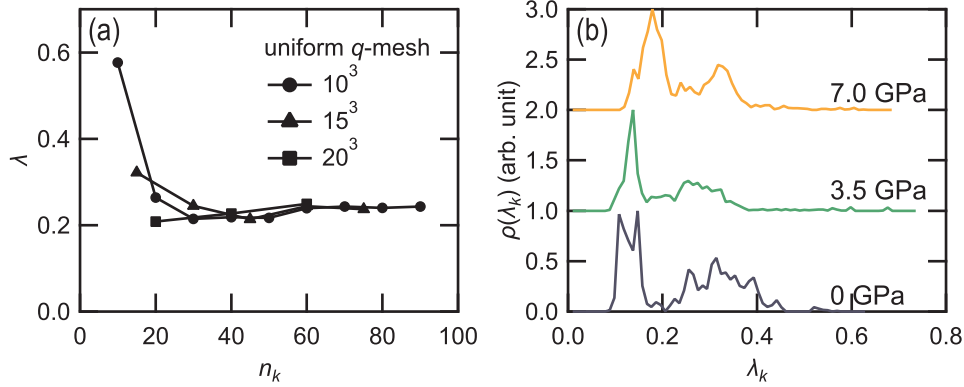


FIG. S12. (a) Electron-phonon coupling strength λ at ambient pressure calculated for various sampling conditions. We used uniform n_k^3 k -meshes. (b) Population ($\rho(\lambda_{\mathbf{k}})$) of the electron-phonon coupling strength ($\lambda_{\mathbf{k}}$) on the Fermi surface. We considered the carriers within the energy range of ± 0.2 eV from the Fermi energy.

indicating that the interpolation procedure works well with sufficient accuracy. The resulting maximally-localized Wannier orbitals at ambient pressure are shown in Fig. S11.

The integrations over the Brillouin zone were performed on uniform 75^3 k -mesh and 15^3 q -mesh [20]. The Dirac delta functions were smeared with widths of 25 meV for electrons and 0.05 meV for phonons. As shown in Fig. S12(a), the adopted meshes were sufficient to obtain the converged λ and were optimal with regard to the computational costs. The distribution of the phonon linewidth $\gamma_{q\nu}$ at each pressure is indicated in Figs. S7–S9(e). By integrating $\gamma_{q\nu}$ over the Brillouin zone according to Eqs. (S9) and (S11), we can obtain the Eliashberg spectral function $\alpha^2 F(\omega)$.

Finally, we show in Fig. S12(b) the population of the electron-phonon coupling strength $\lambda_{\mathbf{k}}$ on the Fermi surface. Here, we consider the carriers within the energy range of ± 0.2 eV from the Fermi energy. We can recognize two distinct peaks at all pressures. The secondary peak at approximately $\lambda_{\mathbf{k}} \sim 0.3$ originates from the carriers on the hollow-like Fermi surface.

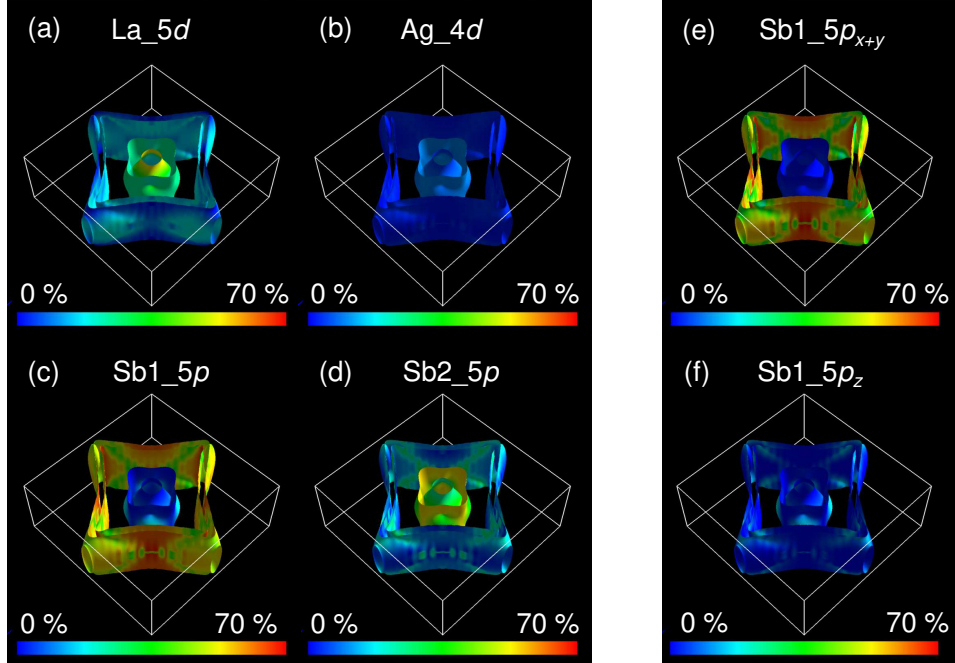


FIG. S13. Projection of (a) La-5*d*, (b) Ag-4*d*, (c) Sb1-5*p*, and (d) Sb2-5*p* characters on the Fermi surface at ambient pressure. Separate views of (e) Sb1-5*p*_{*x+y*} and (f) Sb1-5*p*_{*z*} characters.

VI. ORBITAL CHARACTER OF THE FERMI SURFACE

In Fig. S13, we show the projections of atomic orbitals $|\langle \Psi_{atom,orbital} | \Psi_{n\mathbf{k}} \rangle|^2$ on the Fermi surface at ambient pressure. The calculation was obtained on the 36^3 k -point grid and visualized using FermiSurfer [21]. We plot the projections of representative orbitals having major density of states at the Fermi level, i.e., (a) La-5*d*, (b) Ag-4*d*, (c) Sb1-5*p*, and (d) Sb2-5*p*. Here, Sb1 constitutes the square net layer. We also show in Figs. S13(e) and (f) the details of Sb1-5*p* orbital. The hollow-like Fermi surface is mostly constructed by 5*p*_{*x+y*}, and the contribution of 5*p*_{*z*} is relatively minor.

-
- [1] C. Kittel, *Introduction to Solid State Physics*, 8th ed. (John Wiley & Sons, 2004).
- [2] P. Giannozzi, S. Baroni, N. Bonini, M. Calandra, R. Car, C. Cavazzoni, D. Ceresoli, G. L. Chiarotti, M. Cococcioni, I. Dabo, A. D. Corso, S. de Gironcoli, S. Fabris, G. Fratesi, R. Gebauer, U. Gerstmann, C. Gougoussis, A. Kokalj, M. Lazzeri, L. Martin-Samos, N. Marzari, F. Mauri, R. Mazzarello, S. Paolini, A. Pasquarello, L. Paulatto, C. Sbraccia,

- S. Scandolo, G. Sciauzero, A. P. Seitsonen, A. Smogunov, P. Umari, and R. M. Wentzcovitch, *J. Phys.: Condens. Matter* **21**, 395502 (2009).
- [3] P. Giannozzi, O. Andreussi, T. Brumme, O. Bunau, M. Buongiorno Nardelli, M. Calandra, R. Car, C. Cavazzoni, D. Ceresoli, M. Cococcioni, N. Colonna, I. Carnimeo, A. Dal Corso, S. De Gironcoli, P. Delugas, R. Distasio, A. Ferretti, A. Floris, G. Fratesi, G. Fugallo, R. Gebauer, U. Gerstmann, F. Giustino, T. Gorni, J. Jia, M. Kawamura, H. Ko, A. Kokalj, E. Küçükbenli, M. Lazzeri, M. Marsili, N. Marzari, F. Mauri, N. Nguyen, H. Nguyen, A. Otero-De-La-Roza, L. Paulatto, S. Poncé, D. Rocca, R. Sabatini, B. Santra, M. Schlipf, A. Seitsonen, A. Smogunov, I. Timrov, T. Thonhauser, P. Umari, N. Vast, X. Wu, and S. Baroni, *J. Phys.: Condens. Matter* **29**, 465901 (2017).
- [4] We used `La.pbe-spf-n-rrkjus-ps1.1.0.0.UPF` for La, `Ag.pbe-n-rrkjus-ps1.1.0.0.UPF` for Ag, and `Sb.pbe-n-rrkjus-ps1.1.0.0.UPF` for Sb in `PSlibrary`.
- [5] K. Akiba, H. Nishimori, N. Umeshita, and T. C. Kobayashi, *Phys. Rev. B* **103**, 085134 (2021).
- [6] S. L. Bud'ko, T. A. Wiener, R. A. Ribeiro, P. C. Canfield, Y. Lee, T. Vogt, and A. H. Lacerda, *Phys. Rev. B* **73**, 184111 (2006).
- [7] R. Singha, S. Samanta, T. S. Bhattacharya, S. Chatterjee, S. Roy, L. Wang, A. Singha, and P. Mandal, *Phys. Rev. B* **102**, 205103 (2020).
- [8] M. Kawamura, Y. Gohda, and S. Tsuneyuki, *Phys. Rev. B* **89**, 094515 (2014).
- [9] P. Ruzsala, M. Winiarski, and M. Samsel-Czekala, *Acta Physica Polonica A* **138**, 748 (2020).
- [10] K. Akiba, N. Umeshita, and T. C. Kobayashi, *Phys. Rev. B* **105**, 035108 (2022).
- [11] J. M. Ziman, *Electrons and Phonons: The Theory of Transport Phenomena in Solids* (Oxford University Press, 2001).
- [12] T. Takeuchi, A. Thamizhavel, T. Okubo, M. Yamada, N. Nakamura, T. Yamamoto, Y. Inada, K. Sugiyama, A. Galatanu, E. Yamamoto, K. Kindo, T. Ebihara, and Y. Ōnuki, *Phys. Rev. B* **67**, 064403 (2003).
- [13] G. Pizzi, V. Vitale, R. Arita, S. Bluegel, F. Freimuth, G. Géranton, M. Gibertini, D. Gresch, C. Johnson, T. Koretsune, J. Ibanez, H. Lee, J.-M. Lihm, D. Marchand, A. Marrazzo, Y. Mokrousov, J. I. Mustafa, Y. Nohara, Y. Nomura, L. Paulatto, S. Poncé, T. Ponweiser, J. Qiao, F. Thöle, S. S. Tsirkin, M. Wierzbowska, N. Marzari, D. Vanderbilt, I. Souza, A. A. Mostofi, and J. R. Yates, *J. Phys.: Condens. Matter* **32**, 165902 (2020).
- [14] S. Poncé, E. Margine, C. Verdi, and F. Giustino, *Comput. Phys. Commun.* **209**, 116 (2016).

- [15] W. L. McMillan, Phys. Rev. **167**, 331 (1968).
- [16] R. C. Dynes, Solid State Commun. **10**, 615 (1972).
- [17] P. B. Allen and R. C. Dynes, Phys. Rev. B **12**, 905 (1975).
- [18] P. Morel and P. W. Anderson, Phys. Rev. **125**, 1263 (1962).
- [19] F. Giustino, M. L. Cohen, and S. G. Louie, Phys. Rev. B **76**, 165108 (2007).
- [20] We also confirmed that the calculations converge to almost identical λ using quasi-random 25^3 k - and q -grids.
- [21] M. Kawamura, Comput. Phys. Commun. **239**, 197 (2019).